MATERIALS SCIENCE

Reduced dopant-induced scattering in remote charge-transfer-doped MoS_2 field-effect transistors

Juntae Jang[1]†, Jae-Keun Kim[2]†, Jiwon Shin[1], Jaeyoung Kim[1], Kyeong-Yoon Baek[1], Jaehyoung Park[1], Seungmin Park[3], Young Duck Kim[3], Stuart S. P. Parkin[2], Keehoon Kang[4,5]*, Kyungjune Cho[6]*, Takhee Lee[1,5]*

Efficient doping for modulating electrical properties of two-dimensional (2D) transition metal dichalcogenide (TMDC) semiconductors is essential for meeting the versatile requirements for future electronic and optoelectronic devices. Because doping of semiconductors, including TMDCs, typically involves generation of charged dopants that hinder charge transport, tackling Coulomb scattering induced by the externally introduced dopants remains a key challenge in achieving ultrahigh mobility 2D semiconductor systems. In this study, we demonstrated remote charge transfer doping by simply inserting a hexagonal boron nitride layer between MoS_2 and solution-deposited n-type dopants, benzyl viologen. A quantitative analysis of temperature-dependent charge transport in remotely doped devices supports an effective suppression of the dopant-induced scattering relative to the conventional direct doping method. Our mechanistic investigation of the remote doping method promotes the charge transfer strategy as a promising method for material-level tailoring of electrical and optoelectronic devices based on TMDCs.

INTRODUCTION

Transition metal dichalcogenides (TMDCs), representative two-dimensional (2D) van der Waals (vdW) semiconducting materials, have gained substantial attention because of their attractive material properties, including their ultrathin 2D nature with superior electronic and optoelectronic properties, making them a strong contender for emerging electronics applications (*1*–*11*). In particular, MoS_2, an n-type TMDC semiconductor, has been intensively studied in various research fields because it has shown a wide variety of material properties, not only outstanding MoS_2-based device performances but also strong spin-orbit coupling and valleytronic properties, as well as superconducting properties (*12*–*19*).

To meet the versatile requirements of future electronic and optoelectronic device applications, the electrical properties of TMDCs should ideally be controllable over a wide range on a material level. Doping has been a key element in achieving such control over carrier density, as well as conductivity, and various doping strategies have been developed for expanding the doping range of TMDCs (*20*–*25*). In particular, surface charge transfer doping (SCTD), which involves charge transfer across the interface between TMDCs and externally introduced dopants on the surface, has been intensively studied as an effective method for modulating the electrical properties of TMDCs in a facile manner (*20*). TMDCs, because of their intrinsic 2D nature, can provide a large surface-area-to-volume ratio for highly efficient and sensitive surface charge transfer with dopants adsorbed on the surface. Furthermore, the advantages of SCTD in TMDCs can be amplified by using molecular dopants that can be designed with a high degree of freedom to target dopants with various frontier orbitals and structures for effectively controlling both the carrier type and doping strength (*26*–*28*). Furthermore, the molecular SCTD method in TMDCs occurs via physical adsorption and is believed to have relative advantages in terms of nondestructive and reversible nature over substitutional doping method that involves either a compositional modification during the synthesis (*29*–*31*) or an ion implantation technique (*32*, *33*), both of which accompany structural damages in 2D materials to some extent. An ideal doping method should not only be structurally nondestructive but also be noninvasive in terms of the resulting charge transport (*34*–*36*). Over the past, the concept of spatially separating charged dopants from the conduction channel has been well established as a modulation-doping method (*37*, *38*). This strategy for minimizing dopant-induced scattering effects has realized 2D electron gas in ultrahigh mobility semiconductor systems and has led to the exploration of rich quantum phenomena in 2D, such as quantum Hall effect (*38*, *39*).

Recently, the concept of remote modulation doping in TMDCs has been proposed theoretically by Wang *et al.* (*34*) and demonstrated experimentally by Lee *et al.* (*35*) in a MoS_2/h-BN/WSe_2 heterostructure where the doped WSe_2 acted as the remote source of charges for realizing doping in MoS_2 while suppressing Coulomb scattering by the charged dopants. However, a precise mechanistic understanding of such remote doping strategy and the resulting enhanced charge transport is required for fully using the promising doping method in TMDCs. Accordingly, our recent study on the dopant-induced scattering effects in the charge transport of WSe_2 field-effect transistors (FETs) doped with molecular SCTD can provide a route for gaining additional insights into the remote charge transfer and charged impurity scattering processes (*40*). In this study, we extend our analytical framework to investigate the remote charge transfer doping method quantitatively. We demonstrate that placing only a thin h-BN layer between a MoS_2 conduction channel and solution-deposited molecular dopants is sufficient (i.e., without the WSe_2 for providing the band offsets) for achieving remote charge

[1]Department of Physics and Astronomy, Seoul National University, Seoul 08826, Korea. [2]Max-Planck Institute of Microstructure Physics, Weinberg 2, 06120 Halle, Saale, Germany. [3]Department of Physics, Kyung Hee University, Seoul 02447, Korea. [4]Department of Materials Science and Engineering, Research Institute of Advanced Materials, Seoul National University, Seoul 08826, Korea. [5]Institute of Applied Physics, Seoul National University, Seoul 08826, Korea. [6]Soft Hybrid Materials Research Center, Korea Institute of Science and Technology, Seoul 02792, Korea.
*Corresponding author. Email: keehoon.kang@snu.ac.kr (K.K.); kcho@kist.re.kr (K.C.); tlee@snu.ac.kr (T.L.)
†These authors contributed equally to this work.

transfer in MoS_2, which provides a simple testbed for systematically studying the suppression of charged impurity scattering via temperature-dependent four-point probe transport measurements. As a result, this noninvasive remote doping method was shown to achieve notably higher channel mobility relative to the conventional direct doping method because of a substantially reduced effective-charged impurity density, which is supported by our modified scattering model, as well as a more reliable doping controllability relative to the conventional direct doping method.

RESULTS

h-BN/MoS_2 vdW heterostructure devices for remote charge transfer doping

In this study, our system of interest consists of a MoS_2 channel doped with benzyl viologen (BV) molecules that are spatially separated by an h-BN layer. To demonstrate doping effects in such a system experimentally, we fabricated MoS_2 FET devices with metal contacts for four-point probe measurement, followed by the vdW dry transfer of a thin h-BN layer on the MoS_2 channel area (the fabrication details are provided in Materials and Methods and fig. S1). The device structure of the remotely BV-doped MoS_2 FETs is shown schematically in Fig. 1A. The optical image of a fabricated device before BV deposition is shown in Fig. 1B. An atomic force microscope (AFM) was used to check the surface morphology after a thin h-BN flake was transferred on top of the MoS_2 FET. We could barely observe any blisters or wrinkles in the AFM image (Fig. 1C), indicating that the h-BN was properly transferred and the heterostructure was well formed. The thickness of the MoS_2 channel flake was determined from the AFM image as ~2.7 nm (inset in Fig. 1C and detailed information in fig. S2). The cross-sectional spherical aberration-corrected scanning transmission electron microscopy (Cs-corrected STEM) image of a heterostructure, which confirms the well-stacked h-BN/MoS_2 heterostructures of this particular sample, consisting of five layers of h-BN (~2 nm thick) and four-layers of MoS_2 (~3 nm thick) is shown in Fig. 1D (see fig. S3 for representative device samples). To demonstrate remote charge transfer doping, we specifically selected uniform, large, and especially thin h-BN flakes among the mechanically exfoliated h-BN flakes to cover devices because the thickness of the inserted h-BN layer is a critical factor in determining the remote charge transfer doping efficiency of molecular dopants; the thicker the h-BN layer, the lower the expected doping efficiency. The few-layer MoS_2 channel was selected in this study because of its high surface area–to–volume ratio, which is ideal for investigating the influence of surface-charged impurities generated by the molecular dopants on the charge transport in the remotely doped MoS_2 FETs (*41*).

Charge transfer doping of BV molecules in h-BN/MoS_2 FETs

BV molecule is a strong reductant that has been widely used for SCTD in various nanomaterials as an n-type dopant (*20*, *42*). The molecular structure of the BV molecule and two different charge transfer processes are available for BV molecules (Fig. 2A). As an effective donor, a neutral BV molecule (BV^0) can transfer an electron to an acceptor (in this study, MoS_2), forming a BV^+ cation, which can then be further oxidized to BV^{2+} by transferring another electron to MoS_2. The energy levels of the two redox states of a BV molecule and the corresponding energy levels of h-BN and MoS_2 are illustrated in Fig. 2B. Because the highest occupied molecular orbital (HOMO) of BV is located above the conduction band minimum of MoS_2, it serves as an electron donor (*43*, *44*). We anticipate that charge transfer can occur from molecular dopants to the MoS_2 channel through insulating the h-BN interlayer, provided that the h-BN interlayer is thin enough for sufficient tunneling (Fig. 2B). This remote charge transfer doping strategy enables us to successfully modulate the electrical properties of MoS_2 FETs while minimizing scattering induced by the surface charge dopants.

To confirm the aforementioned remote charge transfer doping in the MoS_2 channel through a thin h-BN flake by BV molecular dopants, we compared the doping effects of direct doping (i.e., dopants deposited directly on the surface of a bare MoS_2 channel) and remote doping (dopants separated from MoS_2 channel by a thin h-BN interlayer) by preparing three different types of MoS_2 FETs: (i) without h-BN encapsulation, (ii) with a thin h-BN layer (<~2 nm), and (iii) with a thick h-BN layer (>~30 nm). Figure 2 (C to E) shows the transfer curves (source-drain current versus gate voltage; I_{DS}-V_{GS}) of MoS_2 FETs without h-BN (Fig. 2C), with a thin h-BN layer (Fig. 2D), and with a thick h-BN layer (Fig. 2E) before BV treatment (pristine) and after BV treatment (BV doped). The transfer curves on the logarithmic scale are provided in the insets of Fig. 2 (C to E). Without the h-BN layer, the transfer curve after direct doping in Fig. 2C shows an increase in current and the shift of the threshold voltages to the negative gate voltage direction, corresponding to the n-doping of MoS_2 (*20*). We could confirm a notable doping effect in the remote charge transfer doping case shown in Fig. 2D, observing a current increase and a similar shift of the threshold voltage to a negative gate voltage direction despite inserting a thin h-BN layer (<~2 nm) between the MoS_2 channel and BV molecules, and spatially separating them from each other. This can be considered analogous to enhanced charge injection from the insertion of a thin h-BN layer between MoS_2 and metal electrodes via tunneling injection rather than hindering the charge injection owing to the insulating nature of the h-BN layer (*45*, *46*). To exclude the possibility that the thin h-BN layer does not encapsulate the device properly so that the BV molecules may directly dope the MoS_2, we examined the electrical hysteresis of the MoS_2 FETs with and without the h-BN layer under ambient conditions. We observed a substantially smaller hysteresis window in the device encapsulated with a thin h-BN flake compared to a bare MoS_2 device (i.e., without the h-BN encapsulation) and confirmed that even a thin h-BN layer could provide enough encapsulation effect (see fig. S4) (*11*). In contrast to the effective charge transfer doping observed for the thin h-BN interlayer, the MoS_2 FET covered with a thick h-BN (>~30 nm; see fig. S5 for more details) demonstrated a noticeably low doping efficiency (Fig. 2E), supporting the critical role of the h-BN thin thickness in achieving substantial doping effects via the remote charge transfer. The thick h-BN interlayer is expected to limit the amount of charge transfer from the BV dopant to the underlying MoS_2 layer. Thus, we confirmed that the exponential decay of Δn (i.e., the doping effect) with increasing thickness of the h-BN interlayer is expected from the decreasing charge tunneling probability through the h-BN interlayer (see fig. S6 for more details). In addition, regarding the stability of the remote doping method, we also characterized the doping stability of the remotely doped devices over time. We confirmed that the remotely doped devices were highly stable under ambient conditions and the remote doping effect in the transfer characteristics were still preserved over time, up to 6 weeks of air exposure (see fig. S7 for more details).

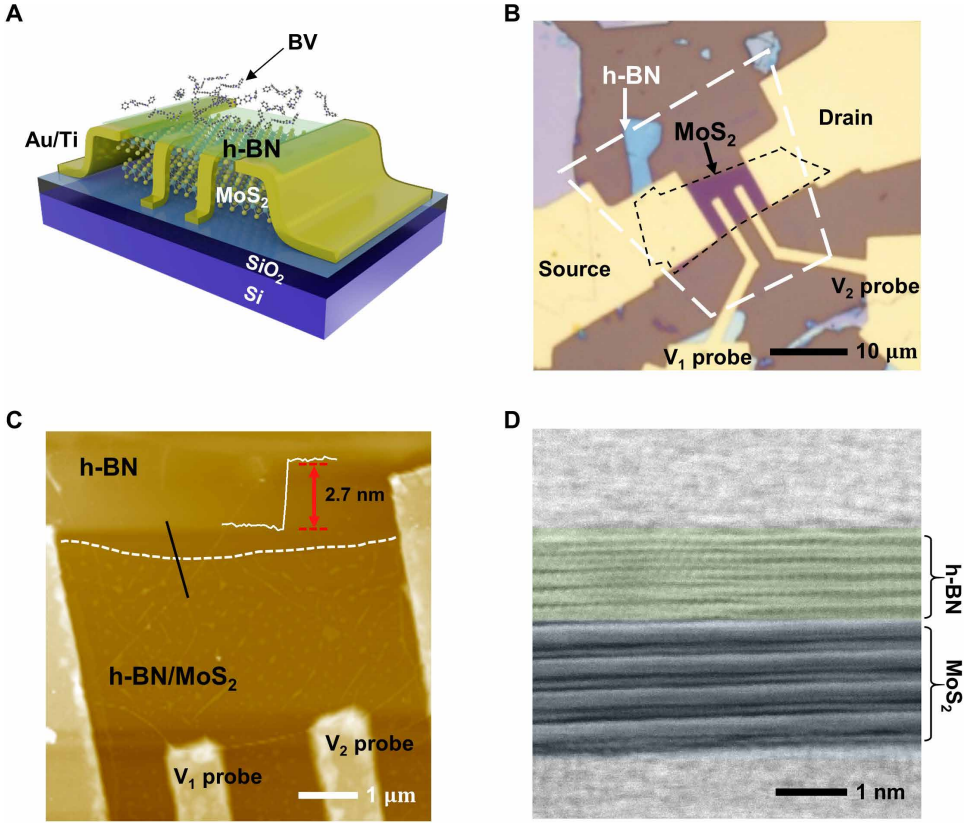

Fig. 1. h-BN/MoS_2 vdW heterostructure devices for remote charge transfer doping. (**A**) The schematic image of BV-doped h-BN/MoS_2 FET with Au/Ti metal contacts for four-point probe measurements. (**B**) Optical image of h-BN/MoS_2 FET before BV doping. (**C**) AFM image of h-BN/MoS_2 FET. The inset shows topographic height profile along the black line, indicating the thickness of the MoS_2 channel of ~2.7 nm. (**D**) Cs-corrected STEM image of the h-BN/MoS_2 heterostructure consisting of five layers of h-BN and four layers of MoS_2.

Doping controllability of remote charge transfer in h-BN/MoS_2 FETs

To apply the remote charge transfer strategy for emerging electronic applications, both doping controllability and available doping range have to be characterized to tailor the electrical properties of the devices by changing dopant density. Therefore, we measured the electrical properties of remotely doped MoS_2 FETs and compared them with the results from un-encapsulated devices by changing the concentration of BV solution from 1 to 10 mM. In particular, we characterized the devices at 10 K in a vacuum to eliminate the contributions of phonon scattering and external defects from the environment toward the overall charge transport.

Because the contact resistance of MoS_2 FETs decreases with BV doping (*20*), we conducted gated four-point probe measurements to focus on the intrinsic charge transport properties of the MoS_2 channel by minimizing the effect of the varying charge injection behavior because of the BV doping (see fig. S8 for more details). Note that the four-point probe measurement analysis required an offset correction because of the measurement setup with limited voltage resolution (see fig. S9 in section S9 for more details). Figure 3 shows the four-point probe conductance (σ_{4pp}) versus gate voltage curves for directly doped (without h-BN) devices (Fig. 3A) and remotely doped (with thin h-BN) devices (Fig. 3B). The measurements were performed on undoped devices (denoted as "pristine") and doped devices with various concentrations of BV solution from 1 to 10 mM. The conductance curves in the logarithmic scale are provided in the insets of Fig. 3 (A and B). As the doping concentration increased in directly doped devices, σ_{4pp} increased and the curves shifted to the negative gate voltage direction, indicating an increase in the degree of n-doping (Fig. 3A). Note that because of the elimination of the contact resistance effects in four-point probe measurements (see fig. S10A), the σ_{4pp} values under the same doping conditions (i.e., same concentration), were higher than the two-point probe conductance (σ_{2pp}) values.

Critically, we repeated the measurements with the remotely doped MoS_2 FETs through a thin h-BN layer, which revealed a similar enhancement in conductance as the doping concentration increased (Fig. 3B). With these results, we can successfully validate the controllability of remote charge transfer doping, which allows us to tailor the electrical properties by varying the dopant solution concentration. Furthermore, our FET characteristics point to clear advantages of remote doping in terms of suppressing dopant-induced scattering effects. The improved σ_{4pp} values that can be observed with remotely doped devices (Fig. 3B) relative to their pristine state could be a sign of a substantially improved mobility of the remotely doped MoS_2 channel compared to that of the directly doped device (Fig. 3A). The difference becomes clear when normalized σ_{4pp} plots of the directly doped and remotely doped devices are used (see fig. S11 for more details). The detailed analysis related to the underlying dopant-induced scattering effect will be discussed in the next sections.

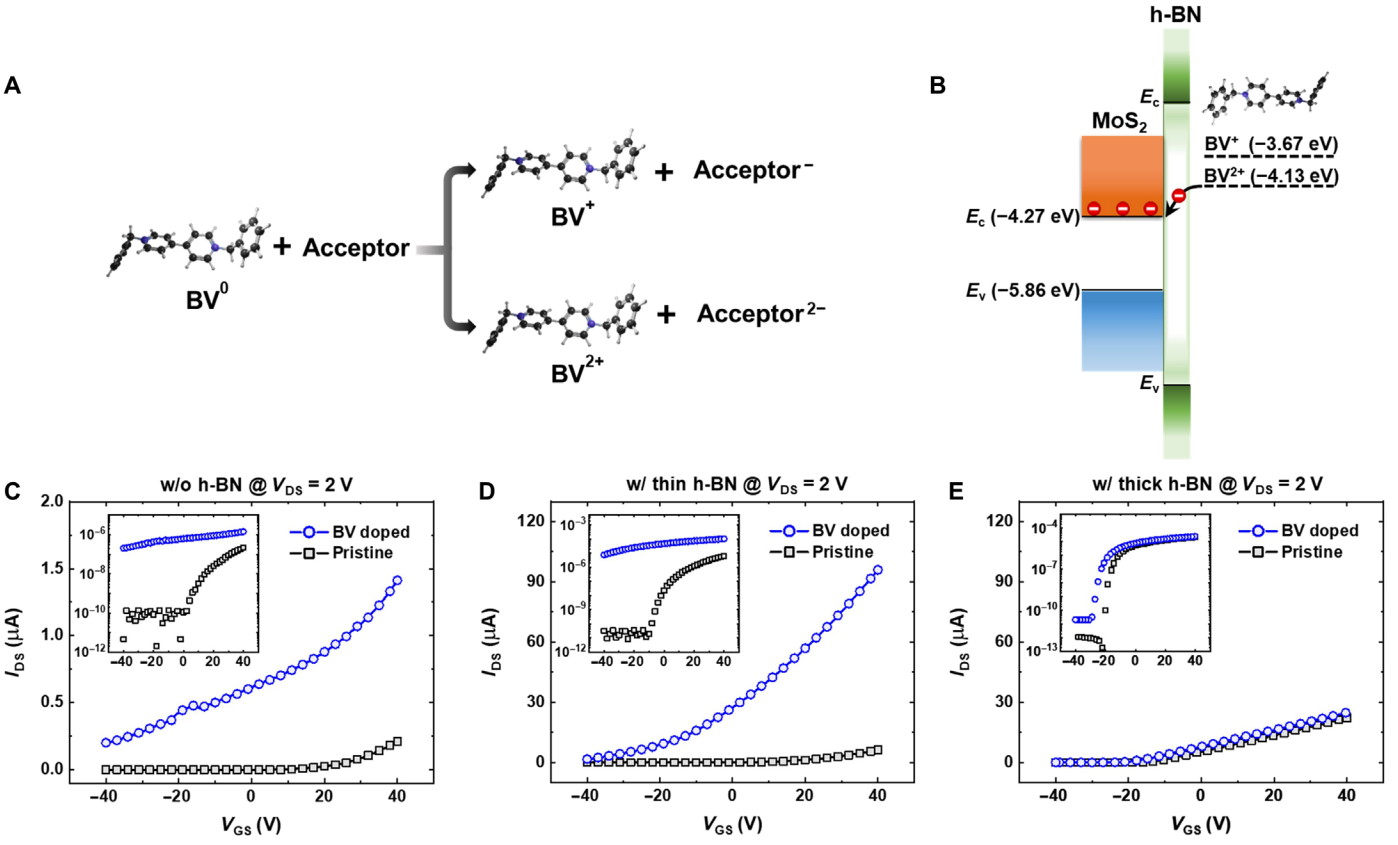

Fig. 2. Charge transfer doping of BV molecules in h-BN/MoS_2 FETs. (**A**) Molecular structure of BV dopant and two different charge transfer doping processes in BV molecules and acceptors (MoS_2). (**B**) HOMO levels of the two redox states of BV molecule and the energy levels of h-BN and MoS_2. (**C** to **E**) I_{DS}-V_{GS} curve of MoS_2 FETs (C) without h-BN and with (D) a thin h-BN (~2 nm) or (E) a thick h-BN layer (>~30 nm), measured at V_{DS} = 2 V before BV treatment (pristine, black squares) and after BV treatment (BV doped, blue circles). The logarithmic scale curves are provided in the insets.

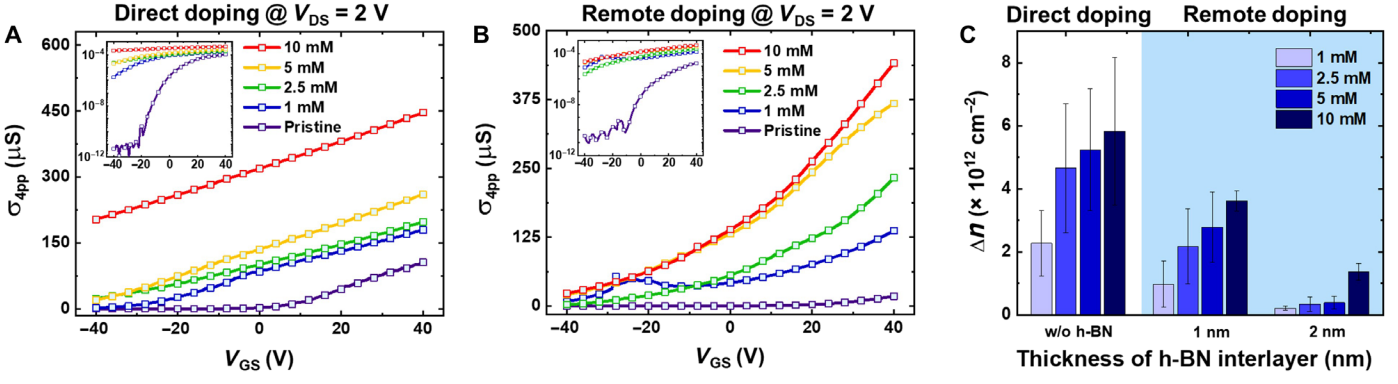

Fig. 3. Doping controllability of remote charge transfer doping in h-BN/MoS_2 FETs. σ_{4pp} versus V_{GS} curves for (**A**) directly doped (without h-BN) devices and (**B**) remotely doped (with thin h-BN) devices with different concentrations of BV solution from 1 to 10 mM at 10 K. The logarithmic scale curves are provided in the insets. (**C**) The amount of increased carrier density (Δn) by doping for different concentrations of BV solution from 1 to 10 mM at 10 K. The left column set represents Δn in directly doped devices. The middle and the right column sets represent Δn in remotely doped devices with a 1-nm-thick and a 2-nm-thick h-BN interlayer, respectively.

To compare the doping strength of direct and remote doping, we extracted the amount of increased carrier density by doping (Δn) using the equation $\Delta n = (C_i \times \Delta V_{th})/q$, where C_i is the capacitance per unit area of the SiO_2 layer ($C_i = 1.3 \times 10^{-4}$ F/m^2), ΔV_{th} ($= V_{th}^{doped} - V_{th}^{pristine}$) is the threshold voltage shift of doped MoS_2 devices relative to the pristine devices, and q is the elementary charge. The obtained Δn values of directly and remotely doped MoS_2 devices are summarized in Fig. 3C. We sorted out the results by h-BN interlayer thickness to investigate the effect of spatial separation between molecular dopants and MoS_2 channels. Note that the largest controllable range of Δn

for direct doping (5.83×10^{12} cm^{-2}) was notably higher than that for remote doping (3.62×10^{12} cm^{-2} for 1-nm h-BN and 1.36×10^{12} cm^{-2} for 2-nm h-BN), implying that the amount of charge transfer decreased in remote doping because of spatial separation. Here, we extracted the largest carrier concentration after doping values, n_{final} values, by using $n_{final} = C_i (V_{GS} - V_{th}^{doped})/q$ at $V_{GS} = 80$ V. It was found that the n_{final} in directly doped devices with 10 mM concentration of BV solution is determined to be 9.02×10^{12} cm^{-2}. In remotely doped devices with 10 mM concentration of BV, the n_{final} is determined to be 6.46×10^{12} cm^{-2} and 3.32×10^{12} cm^{-2} for the devices with 1- and 2-nm h-BN remotely doped devices, respectively (see fig. S12). This result is supported by the smaller controllable range of Δn for the 2-nm h-BN case compared to the 1-nm h-BN case. Overall, the larger spatial separation leads to the smaller amount of charge transfer. The reduced dopant-induced scattering can be expected because of the reduced amount of charge transfer by spatial separation. We will discuss the dopant-induced scattering effect in a later section.

Identifying dopant-induced scattering effects from temperature-dependent mobility measurements

With regard to the mobility of TMDC materials, the mobility can show both increasing and decreasing tendency with carrier density in different carrier density regimes, which originated from various factors, including the screening effect and thickness of TMDCs (*47*–*50*). However, in a well-controlled system that can neglect other factors except for the carrier concentration, Cui *et al.* (*48*) reported that the increased mobility of MoS_2 as carrier density increases because of the enhanced screening of charged impurity potential. It is rational to assume that electrostatic doping by field effect does not introduce additional impurity scattering, whereas the adsorbed dopant molecules on the TMDC surface can act as an additional charged impurity source in SCTD. To effectively control the conductivity of TMDCs via SCTD, it is essential to minimize additional charged impurity scattering that could be introduced by the SCTD. Because remote doping creates a spatial separation between an electronic channel and charged dopants, it can reduce the Coulomb potential from the dopants, resulting in reduced charged impurity scattering. Therefore, the remote doping method can be a suitable candidate for efficiently and reliably controlling the electrical properties of TMDCs.

To investigate the effects of additional introduced charged impurities by adsorbed charge transfer dopants on the surface, the effect of phonon scattering should be excluded by lowering the temperature because charged impurity scattering and phonon scattering are the most dominant sources of charge transport hindrance. Therefore, we performed temperature-dependent gated four-point probe measurements from 10 to 300 K before and after both direct doping and remote doping (see figs. S13 and S14 for representative temperature-dependent conductance plots). Consequently, we extracted the temperature-dependent field-effect mobilities from the directly doped and remotely doped devices and decomposed them to charged impurity scattering–limited mobility and phonon scattering–limited mobility using Matthiessen's rule. Figure 4 shows temperature-dependent field-effect mobilities calculated from the slope of the conductance plots at $V_{GS} = 80$ V for pristine MoS_2 FETs (blue lines) and directly doped and remotely doped MoS_2 FETs (red lines) with a different h-BN interlayer thickness (Fig. 4A for direct doping, Fig. 4B for remote doping with the 1 nm h-BN interlayer, and Fig. 4C for remote doping with the 2-nm h-BN interlayer). It should be noted that the mobility values after doping for all three devices shown in Fig. 4 were extracted under similar Δn conditions ($\Delta n = 0.43$, 0.45, and 0.38×10^{12} cm^{-2}, respectively). The field-effect mobility from four-point probe measurements can be calculated using the following formula

$$\mu_{4pp} = (dG/dV_{GS}) \times (L/WC_i) \quad (1)$$

where G, L, and W denote the conductance, channel length, and channel width, respectively. As shown in Fig. 4, the temperature-dependent mobilities of pristine MoS_2 FETs, and directly and remotely doped MoS_2 FETs increased as the temperature decreased because of suppressed phonon scattering (*51*). According to Matthiessen's rule, the mobility of the channel can be written as

$$\mu_{4pp}(T) = \left(\frac{1}{\mu_C T^{\alpha}} + \frac{1}{\mu_{ph} T^{\beta}} \right)^{-1} \quad (2)$$

where T, μ_c, μ_{ph}, and α and β denote temperature, charged impurity scattering–limited mobility, and phonon-limited mobility at the zero-temperature limit, and their exponents, respectively (*40*, *48*, *52*, *53*). In this analysis, we assumed that the scattering sources, excluding charged impurity and phonon, such as intrinsic defects and the roughness of the substrate, were negligible because the charged impurity and phonon scattering are the most dominant mechanisms in the charge transport of MoS_2, as demonstrated previously (*48*, *51*). In terms of phonon scattering, the β value of the MoS_2 device barely changed upon direct and remote doping compared with those of pristine devices, which suggests that the phonon scattering could be insensitive to the presence of the adsorbed dopants on the MoS_2 surface. In addition, the extracted β value of the remotely doped MoS_2 ($\beta = -1.75$) was slightly lower than that of the directly doped MoS_2 ($\beta = -1.95$; see fig. S15 for more details), indicating that the top h-BN encapsulation can suppress the homopolar phonon scattering because the homopolar phonon mode is considered the most dominant among all phonon modes that contribute to phonon scattering in MoS_2, as reported previously (*54*). The change in the charged impurity scattering–limited mobility ($\mu_c T^{\alpha}$) in mobility after doping can be interpreted by considering two major competing effects: the charge screening effect that enhances the mobility because of a larger screening of Coulomb potential created by the charged impurities (*55*) and larger charged impurity scattering because of a higher dopant ion density as a result of doping, which lowers the mobility because of the numerous charged impurities generated (*40*). In this particular range of doping, the increased mobility after doping indicates a greater screening effect than the scattering effect. Furthermore, previous studies have also shown similar mobility enhancement upon doping in MoS_2 with BV molecules, which supports the observed mobility increase in our directly doped device (*47*–*51*, *55*–*57*).

In comparison, note that the $\mu_c T^{\alpha}$ values of remotely doped MoS_2 devices (Fig. 4, B and C) are greater than that of the directly doped MoS_2 device (Fig. 4A), indicating that the remotely doped devices have a lower degree of charged impurity scattering. In particular, $\mu_c T^{\alpha}$ of remotely doped MoS_2 devices with the 2-nm h-BN interlayer was found to be even larger than that of the 1-nm h-BN case. This could be associated with the spatial separation between the additionally introduced charged impurities (in the form of the adsorbed dopants) and the MoS_2 channel ensured by the thin h-BN interlayer

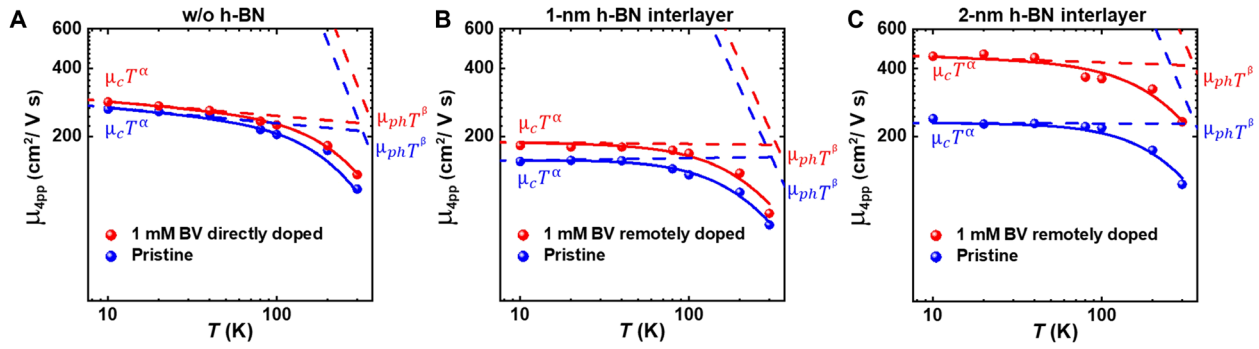

Fig. 4. Temperature-dependent mobility measurements. Temperature-dependent mobility values of (**A**) directly doped, (**B**) remotely doped devices with a 1-nm h-BN interlayer, and (**C**) remotely doped devices with a 2-nm h-BN interlayer at temperatures from 10 to 300 K. The mobility values were extracted from the four-point probe conductance plots at V_{GS} = 80 V for pristine devices (blue lines) and doped devices (red lines) and under similar Δn conditions.

in remote doping, which is expected to induce less Coulomb scattering by charged dopants. It is also meaningful to compare the mobility enhancement under different carrier concentration conditions (i.e., similar carrier concentrations in the pristine state, doped state, and similar Δn). From our comparative analysis (see fig. S16 in section S16), we can deduce that the mobility enhancement of the remotely doped devices would be substantially larger than that of the directly doped devices in all cases. We also compared the mobility versus temperature behavior for directly and remotely doped devices when the screening effect from electrostatically accumulated carriers becomes minimal (i.e., the remaining carriers in the channel are mostly from BV doping; see fig. S17 in section S17 for more details). The relation between mobility and carrier density of MoS_2 for direct and remote doping cases will be discussed in a later section.

Enhanced mobility via suppressed charged impurity scattering in remote doping

The suppressed charged impurity scattering effect observed in the previously discussed remotely doped MoS_2 FETs can be treated in a more quantitative manner. Ong and Fischetti (*58*) proposed a theoretical model for calculating the charged impurity–limited mobility (μ_{imp}) of MoS_2. In the model, the charged impurity scattering rate that is dependent on the charged impurity scattering potential (ϕ^{scr}) determines the charged impurity–limited mobility of MoS_2 FETs. While this model is successful in describing charged impurity scattering in a directly doped TMDC channel where the dopant ions are present on the surface of TMDC (*40*), the model has to be corrected for the remotely doped channel because of the spatial separation introduced by the h-BN interlayer. Considering the spatial separation, which places the charged impurities at a finite distance from the channel, the scattering potential in the model should be modified as the following equation (*59*)

$$\phi_q^{remote} = e^{-qd}\phi_q^{scr} \quad (3)$$

where ϕ_q^{remote} and ϕ_q^{scr} are charged impurity scattering potential in the case of remote doping and direct doping, respectively, d is the h-BN thickness, and q is the scattering vector, defined as the magnitude of the difference in the scattered and initial wave vectors. A detailed discussion of the theoretical models is presented in fig. S18 and section S18.

To compare the experimentally obtained mobility values with the theoretical results, we calculated μ_{imp} as a function of carrier concentration for different impurity concentrations. The plotted lines in Fig. 5 (A and B) are the calculated μ_{imp} curves on the basis of the theoretical simulations in case of direct doping (green lines, Fig. 5A) and remote doping (red and blue lines, Fig. 5B) for different impurity concentrations, respectively. Regarding the remote doping, we plotted blue lines for d = 1 nm and red lines for d = 2 nm. For the experimental values, we used the mobility values at 10 K to minimize the contribution of the phonon scattering and compared only the charged impurity limited mobility. The mobility and carrier density values of directly doped devices are plotted as open circles and remotely doped devices with the 1-nm (2 nm) h-BN interlayer are plotted as blue (red) circles and their pristine values are plotted as blue (red) stars in Fig. 5 (A and B). According to our model, μ_{imp} increases with carrier density in the absence of the h-BN interlayer (i.e., direct doping), and the degree of increase in μ_{imp} decreases gradually (Fig. 5A). In contrast, the μ_{imp} plot for the h-BN case (i.e., remote doping) not only increases monotonically with carrier density but also shows a steeper increase when the spatial separation length, d, increases from 1 to 2 nm (see the blue and red lines for comparison in Fig. 5B, respectively). This shows that the larger spatial separation can further suppress charged impurity scattering, irrespective of the initial charged impurity density corresponding to the mobility values in pristine state. Therefore, unlike in the case of direct doping, the rate of increase in mobility is faster because of a dominant contribution from the charge screening effect as charge density increases.

Experimentally, the mobility values of directly doped MoS_2 devices increased generally with the carrier density of MoS_2, although the mobility values showed some fluctuations as the doping density increased (Fig. 5A). The general increase in the mobility observed in our MoS_2 devices can be attributed to a larger contribution from the screening effect, which increases with doping strength. However, some fluctuations (see brown symbols in Fig. 5A, for example) were observed, which may be a manifestation of a complex interplay between the two competing effects (described above) that vary with doping: screening (i.e., increases mobility) and scattering (i.e., lowers mobility) effects. The observed fluctuations may result from a random nature of the spatial distribution of molecular dopants on the surface of the MoS_2 channel, and they can be even intensified because of the formation of dopant clusters. Because each of these clusters can be treated as a multilayer stacking of the dopant molecules, the

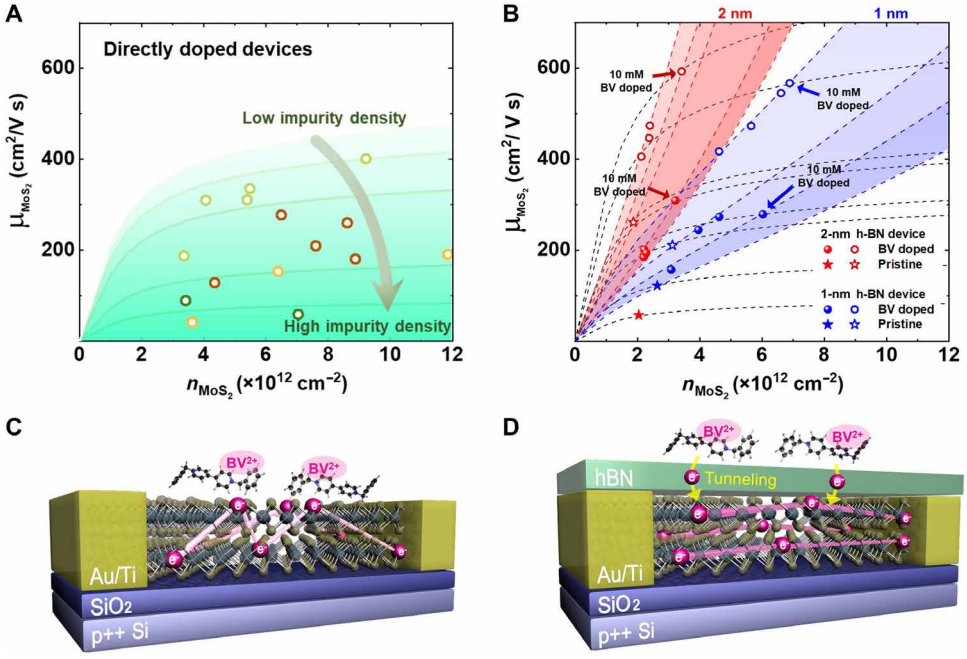

Fig. 5. The suppressed charged impurity scattering effect in the remotely doped MoS_2 FETs. Experimentally determined mobility (μ_{MoS2}) and calculated mobility (μ_{imp}) as a function of carrier concentration (n_{MoS2}). The μ_{imp} values are calculated for (**A**) direct doping (green lines) and (**B**) remote doping (blue lines for the 1-nm h-BN interlayer and red lines for the 2-nm h-BN interlayer) for different impurity concentrations. μ_{MoS2} and n_{MoS2} values of remotely doped devices with the 1-nm (2 nm) h-BN interlayer are plotted as blue (red) circles and their pristine values are plotted as blue (red) stars, determined at 10 K to minimize the contribution of the phonon scattering. (**C**) The schematic images of the directly doped device that suffers from charged impurity scattering. (**D**) The schematic image of the remotely doped device in which the h-BN interlayer suppresses the charged impurity scattering induced by the remote BV^{2+} dopants.

contribution of each dopant layer toward the overall amount of charge transfer (related to the charge screening effect) and degree of charged impurity scattering to the MoS_2 channel would be different (*40*, *60*). To confirm such cluster formation of the BV dopants, we conducted AFM measurements. We could observe that BV dopants (formed as clusters) were distributed non-uniformly on the MoS_2 surfaces, which supports the spatial inhomogeneity of the dopants (see fig. S19 for more details). Therefore, the observed fluctuations in the mobility could be due to complications induced by an unintentional spatial inhomogeneity of the dopants, which apparently limits the reliability of molecular SCTD via direct doping.

In contrast, the experimentally determined mobility of the remotely doped devices demonstrates a steep increase with the carrier density (Fig. 5B), which agrees with our theoretical predictions based on our modified charged impurity scattering model that incorporates the h-BN interlayer (red and blue lines). The steeper slope of the mobility with carrier density in the remotely doped devices relative to the directly doped devices represents a substantially reduced contribution from charged impurity scattering, as the spatial separation of the dopants from the MoS_2 channel reduces the Coulomb potential exerted on the conducting electrons (see Eq. 3).

Although the model developed by Ong and Fischetti (*58*) cannot account for the physical separation of the dopants from the channel in the case of remote doping, it allows us to estimate the effective-charged impurity density (n_{eff}) values for a quantitative comparison of remotely doped devices and directly doped devices. Because of a finite device-to-device variation, it is sensible to compare the change in the dopant-induced charged impurity density by comparing remotely doped devices with similar initial charged impurity density [i.e., a device with $n_{eff} = 0.81 \times 10^{12}$ cm^{-2} (4.00×10^{12} cm^{-2}) indicated as a red open star (red filled star) versus a device with $n_{eff} = 1.21 \times 10^{12}$ cm^{-2} (2.00×10^{12} cm^{-2}) indicated as a blue open star (blue filled star) in Fig. 5B]. The effective charged impurity densities of remotely doped devices (estimated from the fits shown as dashed lines in Fig. 5B) show smaller values (0.54×10^{12} cm^{-2} for 1-nm h-BN and 0.44×10^{12} cm^{-2} for 2-nm h-BN after doping with 10 mM) than those of directly doped devices (1.76×10^{12} cm^{-2} after doping with 10 mM), indicating that the magnitude of charged impurity scattering of remotely doped devices is lower than that of directly doped devices. This suppressed charged impurity scattering can partially account for markedly reduced fluctuations in the mobility curves observed for remote doping; the overall charged impurity scattering is reduced, and thus the varying degrees of charged impurity scattering from the random spatial distribution do not induce noticeable changes in the trend. This also indicates that the remote doping method can be a more reliable method for controlling the electrical properties of MoS_2 devices than the direct doping method, even with solution-based doping methods that suffer from its intrinsically random nature to some extent.

Our discussion can be summarized by the schematic diagrams shown in Fig. 5 (C and D). Unlike the directly doped device, where electron conduction is hampered by the presence of charged BV dopants (BV^{2+}) adsorbed directly on the surface of MoS_2 and acting as charged impurities (Fig. 5C), the presence of the h-BN interlayer suppresses charged impurity scattering from the remote BV^{2+} dopants, thereby demonstrating the noninvasive manner of the remote doping concept presented in our study.

DISCUSSION

In summary, we quantitatively investigated the remote charge transfer doping strategy for demonstrating the suppression of charged impurity scattering in MoS_2 FETs. We realized remote charge transfer in MoS_2 by simply inserting a thin h-BN layer between the MoS_2 channel and molecular dopants, which was sufficient for achieving a notable charge transfer. With this remote charge transfer system, we systematically studied the suppression of the charged impurity scattering via performing temperature-dependent gated four-point probe measurements. As a result, we achieved substantially higher channel mobility, as well as more reliable doping controllability relative to the conventional direct doping method, which is supported by theoretical predictions. We believe that our study will pave the way for fully realizing the potential of remote doping to achieve a wide doping range without compromising the carrier mobility, which is required for high-performance emerging electronic and optoelectronic devices based on 2D vdW materials.

MATERIALS AND METHODS

Device fabrication

MoS_2 and h-BN flakes were mechanically exfoliated from bulk MoS_2 and h-BN crystals and transferred to a 270-nm SiO_2/p++ Si substrate. Suitable MoS_2 and h-BN flakes were located by using an optical microscope, and the thickness of the flakes were measured by an AFM system (NX 10, Park Systems).

After double electron resist layers [methyl methacrylate and poly(methyl methacrylate)] were spin-coated on the MoS_2, the source-drain electrodes were patterned by using an electron beam lithography system (JSM-6510, JEOL). Subsequently, Ti (5 nm)/Au (45 nm) layers were deposited by using an electron-beam evaporator (KVE-2004 L, Korea Vacuum Tech).

To fabricate h-BN/MoS_2 vdW heterostructures, we used the dry-transfer method as follows (*61*). The thin h-BN flakes were picked up by adhesive polycarbonate (purchased from Sigma-Aldrich, PC) deposited on the dome-shaped polydimethylsiloxane stamp. Then, the h-BN flake was placed on top of the fabricated MoS_2 FETs. The heterostructure was dipped into chloroform overnight to remove the remaining polymer residue. Last, we annealed the device at 200°C in an argon atmosphere for 2 hours to improve the interfaces before performing the electrical measurement.

Electrical characterization and temperature-dependent measurements

To confirm SCTD in the MoS_2 devices, two-point probe electrical characterizations were performed in a temperature-variable probe station (MSTECH, M6VC) using a semiconductor parameter analyzer (Keithley 4200-SCS). Keithley 4200-SCS with a pre-amplifier was used to measure the voltage drop across the channel by applying constant dc bias for four-point probe measurements. The temperature-dependent measurements of the directly and remotely doped FETs were carried out with a cryostat system (CS204*I-FMX-12, Advanced Research Systems).

SCTD treatment

We used a drop-casting method with BV solution to perform surface molecular charge transfer doping. For the preparation of the BV solutions, we referred to the previous study (*62*). The BV dichloride (16.35 mg; purchased from Sigma-Aldrich) was dissolved in deionized water (4 ml) and then we added toluene (4 ml; purchased from Sigma-Aldrich). Sequentially, sodium borohydride (40 mg; purchased from Sigma-Aldrich) as a reducing agent was added to the deionized water/toluene layered solution, which was then stirred overnight. While the chemical reaction proceeded, a color change from purple to yellow was observed in the toluene layer. When the chemical reaction was almost completed and the color of the toluene solution was stabilized in yellow, the upper toluene layer was extracted with a micropipette. To conduct the experiments in various doping ranges, we diluted 10 mM BV solution into 1, 2.5, and 5 mM with toluene, respectively. In the drop-casting process, we used 20 μl of the BV solution and we waited for 10 min for the solvent to evaporate under ambient conditions.

SUPPLEMENTARY MATERIALS

Supplementary material for this article is available at https://science.org/doi/10.1126/sciadv.abn3181

REFERENCES AND NOTES

1. Q. H. Wang, K. Kalantar-Zadeh, A. Kis, J. N. Coleman, M. S. Strano, Electronics and optoelectronics of two-dimensional transition metal dichalcogenides. *Nat. Nanotechnol.* **7**, 699–712 (2012).
2. S. Manzeli, D. Ovchinnikov, D. Pasquier, O. V. Yazyev, A. Kis, 2D transition metal dichalcogenides. *Nat. Rev. Mater.* **2**, 17033 (2017).
3. K. F. Mak, C. Lee, J. Hone, J. Shan, T. F. Heinz, Atomically thin MoS_2: A new direct-gap semiconductor. *Phys. Rev. Lett.* **105**, 136805 (2010).
4. Y. L. Huang, Y. Chen, W. Zhang, S. Y. Quek, C.-H. Chen, L.-J. Li, W.-T. Hsu, W.-H. Chang, Y. J. Zheng, W. Chen, A. T. S. Wee, Bandgap tunability at single-layer molybdenum disulphide grain boundaries. *Nat. Commun.* **6**, 6298 (2015).
5. W. Zhang, Q. Wang, Y. Chen, Z. Wang, A. T. S. Wee, Van der Waals stacked 2D layered materials for optoelectronics. *2D Mater.* **3**, 022001 (2016).
6. C.-H. Lee, G.-H. Lee, A. M. van der Zande, W. Chen, Y. Li, M. Han, X. Cui, G. Arefe, C. Nuckolls, T. F. Heinz, J. Guo, J. Hone, P. Kim, Atomically thin p–n junctions with van der Waals heterointerfaces. *Nat. Nanotechnol.* **9**, 676–681 (2014).
7. M. E. Beck, M. C. Hersam, Emerging opportunities for electrostatic control in atomically thin devices. *ACS Nano* **14**, 6498–6518 (2020).
8. J. Xu, L. Chen, Y.-W. Dai, Q. Cao, Q.-Q. Sun, S.-J. Ding, H. Zhu, D. W. Zhang, A two-dimensional semiconductor transistor with boosted gate control and sensing ability. *Sci. Adv.* **3**, e1602246 (2017).
9. D.-H. Lien, S. Z. Uddin, M. Yeh, M. Amani, H. Kim, J. W. Ager III, E. Yablonovitch, A. Javey, Electrical suppression of all nonradiative recombination pathways in monolayer semiconductors. *Science* **364**, 468–471 (2019).
10. H. Kim, S. Z. Uddin, N. Higashitarumizu, E. Rabani, A. Javey, Inhibited nonradiative decay at all exciton densities in monolayer semiconductors. *Science* **373**, 448–452 (2021).
11. J. Shim, S.-H. Bae, W. Kong, D. Lee, K. Qiao, D. Nezich, J. Park Yong, R. Zhao, S. Sundaram, X. Li, H. Yeon, C. Choi, H. Kum, R. Yue, G. Zhou, Y. Ou, K. Lee, J. Moodera, X. Zhao, J.-H. Ahn, C. Hinkle, A. Ougazzaden, J. Kim, Controlled crack propagation for atomic precision handling of wafer-scale two-dimensional materials. *Science* **362**, 665–670 (2018).
12. S. B. Desai, S. R. Madhvapathy, A. B. Sachid, J. P. Llinas, Q. Wang, G. H. Ahn, G. Pitner, M. J. Kim, J. Bokor, C. Hu, H.-S. P. Wong, A. Javey, MoS_2 transistors with 1-nanometer gate lengths. *Science* **354**, 99–102 (2016).
13. B. Radisavljevic, A. Radenovic, J. Brivio, V. Giacometti, A. Kis, Single-layer MoS_2 transistors. *Nat. Nanotechnol.* **6**, 147–150 (2011).
14. J. G. Roch, G. Froehlicher, N. Leisgang, P. Makk, K. Watanabe, T. Taniguchi, R. J. Warburton, Spin-polarized electrons in monolayer MoS_2. *Nat. Nanotechnol.* **14**, 432–436 (2019).
15. K. F. Mak, K. L. McGill, J. Park, P. L. McEuen, The valley hall effect in MoS_2 transistors. *Science* **344**, 1489–1492 (2014).
16. J. M. Lu, O. Zheliuk, I. Leermakers, N. F. Q. Yuan, U. Zeitler, K. T. Law, J. T. Ye, Evidence for two-dimensional ising superconductivity in gated MoS_2. *Science* **350**, 1353–1357 (2015).
17. Y. Saito, Y. Nakamura, M. S. Bahramy, Y. Kohama, J. Ye, Y. Kasahara, Y. Nakagawa, M. Onga, M. Tokunaga, T. Nojima, Y. Yanase, Y. Iwasa, Superconductivity protected by spin–valley locking in ion-gated MoS_2. *Nat. Phys.* **12**, 144–149 (2016).
18. X. Liu, M. C. Hersam, 2D materials for quantum information science. *Nat. Rev. Mater.* **4**, 669–684 (2019).
19. A. Aljarb, J.-H. Fu, C.-C. Hsu, C.-P. Chuu, Y. Wan, M. Hakami, D. R. Naphade, E. Yengel, C.-J. Lee, S. Brems, T.-A. Chen, M.-Y. Li, S.-H. Bae, W.-T. Hsu, Z. Cao, R. Albaridy, S. Lopatin,

W.-H. Chang, T. D. Anthopoulos, J. Kim, L.-J. Li, V. Tung, Ledge-directed epitaxy of continuously self-aligned single-crystalline nanoribbons of transition metal dichalcogenides. *Nat. Mater.* **19**, 1300–1306 (2020).
20. D. Kiriya, M. Tosun, P. Zhao, J. S. Kang, A. Javey, Air-stable surface charge transfer doping of MoS_2 by benzyl viologen. *J. Am. Chem. Soc.* **136**, 7853–7856 (2014).
21. B. Radisavljevic, A. Kis, Mobility engineering and a metal–insulator transition in monolayer MoS_2. *Nat. Mater.* **12**, 815–820 (2013).
22. S. Mouri, Y. Miyauchi, K. Matsuda, Tunable photoluminescence of monolayer MoS_2 via chemical doping. *Nano Lett.* **13**, 5944–5948 (2013).
23. L. Yang, K. Majumdar, H. Liu, Y. Du, H. Wu, M. Hatzistergos, P. Y. Hung, R. Tieckelmann, W. Tsai, C. Hobbs, P. D. Ye, Chloride molecular doping technique on 2D materials: WS_2 and MoS_2. *Nano Lett.* **14**, 6275–6280 (2014).
24. H. Fang, S. Chuang, T. C. Chang, K. Takei, T. Takahashi, A. Javey, High-performance single layered WSe_2 p-FETs with chemically doped contacts. *Nano Lett.* **12**, 3788–3792 (2012).
25. H. Fang, M. Tosun, G. Seol, T. C. Chang, K. Takei, J. Guo, A. Javey, Degenerate n-doping of few-layer transition metal dichalcogenides by potassium. *Nano Lett.* **13**, 1991–1995 (2013).
26. S. Zhang, H. M. Hill, K. Moudgil, C. A. Richter, A. R. H. Walker, S. Barlow, S. R. Marder, C. A. Hacker, S. J. Pookpanratana, Controllable, wide-ranging n-doping and p-doping of monolayer group 6 transition-metal disulfides and diselenides. *Adv. Mater.* **30**, 1802991 (2018).
27. M.-Y. Tsai, S. Zhang, P. M. Campbell, R. R. Dasari, X. Ba, A. Tarasov, S. Graham, S. Barlow, S. R. Marder, E. M. Vogel, Solution-processed doping of trilayer WSe_2 with redox-active molecules. *Chem. Mater.* **29**, 7296–7304 (2017).
28. S. A. Paniagua, J. Baltazar, H. Sojoudi, S. K. Mohapatra, S. Zhang, C. L. Henderson, S. Graham, S. Barlow, S. R. Marder, Production of heavily n- and p-doped CVD graphene with solution-processed redox-active metal–organic species. *Mater. Horiz.* **1**, 111–115 (2014).
29. H. Gao, J. Suh, M. C. Cao, A. Y. Joe, F. Mujid, K.-H. Lee, S. Xie, P. Poddar, J.-U. Lee, K. Kang, P. Kim, D. A. Muller, J. Park, Tuning electrical conductance of MoS_2 Monolayers through substitutional doping. *Nano Lett.* **20**, 4095–4101 (2020).
30. T. Zhang, K. Fujisawa, F. Zhang, M. Liu, M. C. Lucking, R. N. Gontijo, Y. Lei, H. Liu, K. Crust, T. Granzier-Nakajima, H. Terrones, A. L. Elías, M. Terrones, Universal in situ substitutional doping of transition metal dichalcogenides by liquid-phase precursor-assisted synthesis. *ACS Nano* **14**, 4326–4335 (2020).
31. S. K. Pandey, H. Alsalman, J. G. Azadani, N. Izquierdo, T. Low, S. A. Campbell, Controlled p-type substitutional doping in large-area monolayer WSe_2crystals grown by chemical vapor deposition. *Nanoscale* **10**, 21374–21385 (2018).
32. V. Iberi, L. Liang, A. V. Ievlev, M. G. Stanford, M.-W. Lin, X. Li, M. Mahjouri-Samani, S. Jesse, B. G. Sumpter, S. V. Kalinin, D. C. Joy, K. Xiao, A. Belianinov, O. S. Ovchinnikova, Nanoforging single layer $MoSe_2$ through defect engineering with focused helium ion beams. *Sci. Rep.* **6**, 30481 (2016).
33. K. Xu, Y. Zhao, Z. Lin, Y. Long, Y. Wang, M. Chan, Y. Chai, Doping of two-dimensional MoS_2 by high energy ion implantation. *Semicond. Sci. Technol.* **32**, 124002 (2017).
34. D. Wang, X.-B. Li, H.-B. Sun, Modulation doping: A strategy for 2D materials electronics. *Nano Lett.* **21**, 6298–6303 (2021).
35. D. Lee, J. J. Lee, Y. S. Kim, Y. H. Kim, J. C. Kim, W. Huh, J. Lee, S. Park, H. Y. Jeong, Y. D. Kim, C.-H. Lee, Remote modulation doping in van der Waals heterostructure transistors. *Nat. Electron.* **4**, 664–670 (2021).
36. K. Kang, S. Watanabe, K. Broch, A. Sepe, A. Brown, I. Nasrallah, M. Nikolka, Z. Fei, M. Heeney, D. Matsumoto, K. Marumoto, H. Tanaka, S.-i. Kuroda, H. Sirringhaus, 2D coherent charge transport in highly ordered conducting polymers doped by solid state diffusion. *Nat. Mater.* **15**, 896–902 (2016).
37. E. F. Schubert, Doping in heterostructures, quantum wells, and superlattices, in *Doping in III-V Semiconductors* (Cambridge Univ. Press, 1993), pp. 392–397.
38. H. L. Störmer, The fractional quantum hall effect, in *Advances in Solid State Physics* (Springer Berlin Heidelberg, 1984), vol. 24, pp. 25–44.
39. G. Springholz, G. Ihninger, G. Bauer, M. M. Olver, J. Z. Pastalan, S. Romaine, B. B. Goldberg, Modulation doping and observation of the integral quantum Hall effect in PbTe/$Pb_{1-x}Eu_xTe$ multiquantum wells. *Appl. Phys. Lett.* **63**, 2908–2910 (1993).
40. J.-K. Kim, K. Cho, J. Jang, K.-Y. Baek, J. Kim, J. Seo, M. Song, J. Shin, J. Kim, S. S. P. Parkin, J.-H. Lee, K. Kang, T. Lee, Molecular dopant-dependent charge transport in surface-charge-transfer-doped tungsten diselenide field effect transistors. *Adv. Mater.* **33**, 2101598 (2021).
41. S.-L. Li, K. Komatsu, S. Nakaharai, Y.-F. Lin, M. Yamamoto, X. Duan, K. Tsukagoshi, Thickness scaling effect on interfacial barrier and electrical contact to two-dimensional MoS_2 layers. *ACS Nano* **8**, 12836–12842 (2014).
42. B. Chamlagain, S. S. Withanage, A. C. Johnston, S. I. Khondaker, Scalable lateral heterojunction by chemical doping of 2D TMD thin films. *Sci. Rep.* **10**, 12970 (2020).
43. C. Gong, H. Zhang, W. Wang, L. Colombo, R. M. Wallace, K. Cho, Band alignment of two-dimensional transition metal dichalcogenides: Application in tunnel field effect transistors. *Appl. Phys. Lett.* **103**, 053513 (2013).
44. F. Zhao, Q. Li, K. Han, T. Lian, Mechanism of efficient viologen radical generation by ultrafast electron transfer from cds quantum dots. *J. Phys. Chem. C* **122**, 17136–17142 (2018).
45. J. Wang, Q. Yao, C.-W. Huang, X. Zou, L. Liao, S. Chen, Z. Fan, K. Zhang, W. Wu, X. Xiao, C. Jiang, W.-W. Wu, High mobility MoS_2 transistor with low schottky barrier contact by using atomic thick h-BN as a tunneling layer. *Adv. Mater.* **28**, 8302–8308 (2016).
46. Y. Liu, H. Wu, H.-C. Cheng, S. Yang, E. Zhu, Q. He, M. Ding, D. Li, J. Guo, N. O. Weiss, Y. Huang, X. Duan, Toward barrier free contact to molybdenum disulfide using graphene electrodes. *Nano Lett.* **15**, 3030–3034 (2015).
47. A. Allain, A. Kis, Electron and hole mobilities in single-layer WSe_2. *ACS Nano* **8**, 7180–7185 (2014).
48. X. Cui, G.-H. Lee, Y. D. Kim, G. Arefe, P. Y. Huang, C.-H. Lee, D. A. Chenet, X. Zhang, L. Wang, F. Ye, F. Pizzocchero, B. S. Jessen, K. Watanabe, T. Taniguchi, D. A. Muller, T. Low, P. Kim, J. Hone, Multi-terminal transport measurements of MoS_2 using a van der Waals heterostructure device platform. *Nat. Nanotechnol.* **10**, 534–540 (2015).
49. S.-L. Li, K. Wakabayashi, Y. Xu, S. Nakaharai, K. Komatsu, W.-W. Li, Y.-F. Lin, A. Aparecido-Ferreira, K. Tsukagoshi, Thickness-dependent interfacial Coulomb scattering in atomically thin field-effect transistors. *Nano Lett.* **13**, 3546–3552 (2013).
50. N. R. Pradhan, D. Rhodes, S. Memaran, J. M. Poumirol, D. Smirnov, S. Talapatra, S. Feng, N. Perea-Lopez, A. L. Elias, M. Terrones, P. M. Ajayan, L. Balicas, Hall and field-effect mobilities in few layered p-WSe_2 field-effect transistors. *Sci. Rep.* **5**, 8979 (2015).
51. N. Ma, D. Jena, Charge scattering and mobility in atomically thin semiconductors. *Phy. Rev. X* **4**, 011043 (2014).
52. A. T. Neal, H. Liu, J. Gu, P. D. Ye, Magneto-transport in MoS_2: Phase coherence, spin–orbit scattering, and the hall factor. *ACS Nano* **7**, 7077–7082 (2013).
53. B. W. H. Baugher, H. O. H. Churchill, Y. Yang, P. Jarillo-Herrero, Intrinsic electronic transport properties of high-quality monolayer and bilayer MoS_2. *Nano Lett.* **13**, 4212–4216 (2013).
54. K. Kaasbjerg, K. S. Thygesen, K. W. Jacobsen, Phonon-limited mobility in *n*-type single-layer MoS_2 from first principles. *Phys. Rev. B* **85**, 115317 (2012).
55. A. Rai, A. Valsaraj, H. C. Movva, A. Roy, R. Ghosh, S. Sonde, S. Kang, J. Chang, T. Trivedi, R. Dey, S. Guchhait, S. Larentis, L. F. Register, E. Tutuc, S. K. Banerjee, Air stable doping and intrinsic mobility enhancement in monolayer molybdenum disulfide by amorphous titanium suboxide encapsulation. *Nano Lett.* **15**, 4329–4336 (2015).
56. H. G. Ji, P. Solís-Fernández, D. Yoshimura, M. Maruyama, T. Endo, Y. Miyata, S. Okada, H. Ago, Chemically tuned p- and n-type WSe_2 monolayers with high carrier mobility for advanced electronics. *Adv. Mater.* **31**, 1903613 (2019).
57. D. Lembke, A. Allain, A. Kis, Thickness-dependent mobility in two-dimensional MoS_2 transistors. *Nanoscale* **7**, 6255–6260 (2015).
58. Z.-Y. Ong, M. V. Fischetti, Mobility enhancement and temperature dependence in top-gated single-layer MoS_2. *Phys. Rev. B* **88**, 165316 (2013).
59. X. Liu, Z. Wang, K. Watanabe, T. Taniguchi, O. Vafek, J. I. A. Li, Tuning electron correlation in magic-angle twisted bilayer graphene using Coulomb screening. *Science* **371**, 1261–1265 (2021).
60. M. Yarali, Y. Zhong, S. N. Reed, J. Wang, K. A. Ulman, D. J. Charboneau, J. B. Curley, D. J. Hynek, J. V. Pondick, S. Yazdani, N. Hazari, S. Y. Quek, H. Wang, J. J. Cha, Near-unity molecular doping efficiency in monolayer MoS_2. *Adv. Electron. Mater.* **7**, 2000873 (2021).
61. D. G. Purdie, N. M. Pugno, T. Taniguchi, K. Watanabe, A. C. Ferrari, A. Lombardo, Cleaning interfaces in layered materials heterostructures. *Nat. Commun.* **9**, 5387 (2018).
62. S. M. Kim, J. H. Jang, K. K. Kim, H. K. Park, J. J. Bae, W. J. Yu, I. H. Lee, G. Kim, D. D. Loc, U. J. Kim, E.-H. Lee, H.-J. Shin, J.-Y. Choi, Y. H. Lee, Reduction-controlled viologen in bisolvent as an environmentally stable n-type dopant for carbon nanotubes. *J. Am. Chem. Soc.* **131**, 327–331 (2009).
63. W. Park, J. Park, J. Jang, H. Lee, H. Jeong, K. Cho, S. Hong, T. Lee, Oxygen environmental and passivation effects on molybdenum disulfide field effect transistors. *Nanotechnology* **24**, 095202 (2013).
64. K. Cho, W. Park, J. Park, H. Jeong, J. Jang, T.-Y. Kim, W. K. Hong, S. Hong, T. Lee, Electric stress-induced threshold voltage instability of multilayer MoS_2 field effect transistors. *ACS Nano* **7**, 7751–7758 (2013).
65. J. G. Simmons, Generalized formula for the electric tunnel effect between similar electrodes separated by a thin insulating film. *J. Appl. Phys.* **34**, 1793–1803 (1963).
66. S.-L. Li, K. Tsukagoshi, E. Orgiu, P. Samori, Charge transport and mobility engineering in two-dimensional transition metal chalcogenide semiconductors. *Chem. Soc. Rev.* **45**, 118–151 (2016).

Acknowledgments

Funding: We appreciate the financial support of the National Research Foundation of Korea (NRF) grant (nos. 2021R1A2C3004783 and NRF-2021R1C1C1010266), the Nano•Material Technology Development Program grant (no. 2021M3H4A1A02049651), and the BrainLink program (no. 2022H1D3A3A01077343) through NRF funded by the Ministry of Science and ICT of Korea. K.C. appreciates the support of the NRF grant funded by the Korean government (MSIT) (no.2021R1C1C2091728). S.P. and Y.D.K. acknowledge support from the NRF of Korea

(nos. 2021R1A2C2093155 and 2021M3H4A1A03054856). We acknowledge support from the National Center for Inter-University Research Facilities (NCIRF) at Seoul National University for the Cs-corrected scanning transmission electron microscopy measurements performed in this work. **Author contributions:** J.J., J.-K.K., K.K., and T.L. conceived the idea and designed the experiments. J.J. fabricated the devices and performed the electrical measurements and data analysis. J.S., J.K., and J.P. assisted with finding the suitable MoS_2 and h-BN flakes and supported the thickness determination by AFM. S.P. and Y.D.K. advised dry-transfer method for device fabrication. J.J., K.-Y.B., and K.C. designed and arranged the figures. S.S.P.P. advised the scientific discussion on this research. T.L. supervised this research. The manuscript was prepared by J.J., J.-K.K., K.K., K.C., and T.L. with input from all authors. **Competing interests:** The authors declare that they have no competing interests. **Data and materials availability:** All data needed to evaluate the conclusions in the paper are present in the paper and/or the Supplementary Materials.

Submitted 18 November 2021
Accepted 10 August 2022
Published 21 September 2022
10.1126/sciadv.abn3181

Science Advances

Reduced dopant-induced scattering in remote charge-transfer-doped MoS2 field-effect transistors

Juntae JangJae-Keun KimJiwon ShinJaeyoung KimKyeong-Yoon BaekJaehyoung ParkSeungmin ParkYoung Duck KimStuart S. P. ParkinKeehoon KangKyungjune ChoTakhee Lee

Sci. Adv., 8 (38), eabn3181. • DOI: 10.1126/sciadv.abn3181